Materials Horizons

ROYAL SOCIETY OF CHEMISTRY

COMMUNICATION

View Article Online
View Journal | View Issue

Cite this: *Mater. Horiz.*, 2020, 7, 855

Received 12th September 2019,
Accepted 27th November 2019

DOI: 10.1039/c9mh01443h

rsc.li/materials-horizons

All-weather-available, continuous steam generation based on the synergistic photo-thermal and electro-thermal conversion by MXene-based aerogels†

Xing Zhao,‡ Li-Mei Peng,‡ Chun-Yan Tang, Jun-Hong Pu, Xiang-Jun Zha, Kai Ke, Rui-Ying Bao, Ming-Bo Yang and Wei Yang *

Solar energy triggered steam generation has emerged as a green and sustainable strategy that can potentially address the long-standing global freshwater scarcity issue. However, given that there is inadequate light illumination early in the morning or late afternoon or cloudy days, it is continuous steam generation in all weather that is a great challenge for the state-of-the-art solar-driven steam generators. Here, we present an all-weather-available steam generation system, which is capable of harvesting solar energy to continuously generate steam based on the alternative photo-thermal and electro-thermal conversion of crosslinked MXene aerogels (CMAs) in the day time and at night. In virtue of the strong light absorption and excellent electrical conductivity of the CMA, the constructed steam generation system can not only convert sunlight into heat for steam generation on sunny days but persistently achieve heat generation by utilization of electricity in low-light or dark circumstances. Furthermore, the ingenious introduction of solar cells-battery components makes full use of the daytime sunlight to further power the steam generation system for heating up the CMA at night, avoiding extra electrical energy input and loss. This work offers new insights into developing continuous steam generation technologies applicable to day–night alternation and complex environments.

New concepts

The shortage of available drinking water resources is increasingly becoming an urgent worldwide problem. As a ubiquitous solar–thermal energy conversion process, solar-driven interfacial evaporation has attracted tremendous attention owing to its high conversion efficiency of solar energy and transformative industrial potential, and can potentially address the long-standing global clean water scarcity issue. However, given that there is inadequate light illumination early in the morning or late afternoon or cloudy days, it is a great challenge to generate steam continuously in all weather for the state-of-the-art solar-driven steam generators. In this work, we have developed an all-weather and continuous steam generation system based on 3D MXene-based aerogels. Combined with solar cells-battery (SC-B) components, the well-designed steam generation system demonstrates all-weather steam generation, where the CMA can convert sunlight into heat for steam generation and the SC-B can convert sunlight into electricity on sunny days to further power the CMA for electro-thermal steam generation in gloomy weather and dark conditions. This work offers new insights into developing continuous steam generation technologies applicable to day–night alternation and any complex environments for practical applications.

1. Introduction

As a clean, renewable, and environment-friendly technology, solar radiation has high potential in steam generation regarding converting abundant solar energy into heat for freshwater production, thus it is expected to address the worldwide freshwater resource shortage issue.[1–3] Since Chen *et al.* proposed the heat localization concept in 2014, solar-driven interfacial evaporation has drawn much attention due to the relatively higher solar-thermal conversion efficiency.[4] Over the past 5 years, a lot of efforts have been devoted to further improving the water evaporation rate and energy conversion efficiency by innovations from photo-thermal material designs to water transportation structure designs.[5–10] However, almost all reported solar evaporators can only effectively generate steam in sunny days with strong sunlight exposure.[11–13] When exposed to weak sunlight such as rainy, foggy, cloudy or dark environments, the solar-triggered water evaporator is almost down for steam generation, severely limiting the total amount of produced clean water.[14] As every year for more than half of the time many areas on the Earth receive poor or no solar radiation, it is of great significance to design steam generators for persistent steam generation in all circumstances.

With the aim of significantly improving clean water production, all-weather steam generators are promising to meet the escalating freshwater demand. To address this profound issue, we developed a new steam generation system by integrating an

College of Polymer Science and Engineering, Sichuan University, State Key Laboratory of Polymer Materials Engineering, Chengdu, 610065, Sichuan, China. E-mail: weiyang@scu.edu.cn; Fax: +86 28 8546 0130; Tel: +86 28 8546 0130

† Electronic supplementary information (ESI) available. See DOI: 10.1039/c9mh01443h

‡ Xing Zhao and Li-Mei Peng contributed equally to this work.

efficient light-absorption material for steam generation on sunny days with solar cells-battery components for powering the light-absorption material to generate steam in low-light environments. In this prototype, a single material with both high light absorption efficiency and excellent electrical conductivity is desirable for practical all-weather steam generation application. In a typical electro-thermal process, it is essential to have a lower electrical resistance which ensures a lower voltage input to generate enough heat for all-weather steam generation. So far, various photo-thermal materials, such as metallic nanoparticles,[15,16] carbon materials,[17–20] semiconductors,[21–24] polymers,[25–28] inorganics[29,30] and biomass materials,[31] have been employed to achieve efficient solar-steam conversion. However, it remains a great challenge to achieve remarkable electrical conductivity in the foregoing photo-thermal materials (except for metals and carbon materials). Some noble metals, such as silver nanowires, exhibit excellent electrical performance, though most of them suffer from limitations due to high cost and complex manufacturing techniques.[32] Carbon materials, such as graphene and carbon nanotubes, have inherently high electrical conductivity, while it is difficult to obtain porous, highly conductive monolithic carbonaceous materials with superb hydrophilicity using current assembly techniques.[33] Therefore, there is an urgent need to develop novel monolithic porous materials in conjunction with features of hydrophilicity, high electrical conductivity and high light absorption performance.

MXenes, with the chemical formula of $M_{n+1}X_nT_x$, where M represents an early transition metal, X is carbon and/or nitrogen and T_x refers to surface functional groups, as a new family of multifunctional 2D materials with many attractive and tunable properties,[34] have been developed by Gogotsi, Barsoum, and colleagues.[35,36] The unique structure and distinctive surface chemistry endow MXenes with many key properties, such as metallic conductivity and hydrophilic surfaces.[37–39] The integration of 2D materials into 3D macroscopic structures, such as porous films, scaffolds and networks, is highly probable to provide a good solution to the issue of poor light absorption and slow water transportation in steam generators, thereby leading to high-performance steam generation.[40–43] Strategies including a sacrificial template method,[44] introduction of interlayer spacers,[45,46] and an *in situ* foaming process[47] have been proposed to obtain highly electrically conductive MXene porous structures. However, poor mechanical stability severely limits their practical applications. Graphene oxide (GO) assisted hydrothermal assembly was also employed to construct rGO/MXene hybrid porous aerogels.[48–52] However, the presence of large amounts of GO or rGO (*ca.* >30%) severely reduces their electrical conductivities. As MXenes are rigid flakes with a small size, it is still a big challenge to construct highly electrically conductive porous 3D MXene architectures with the aid of only a small amount of GO (*ca.* <10%).

Herein, we report a facile co-gelation strategy to assemble 2D MXene sheets into highly conductive, light-absorbing, thermally insulating, and hydrophilic 3D porous architectures with a small amount of GO by using ethylenediamine (EDA) as a crosslinker. With the aid of freeze drying, the crosslinked MXene hydrogels (CMHs) became crosslinked MXene aerogels (CMAs). The well-designed steam generation system based on the CMAs and solar cells-battery (SC-B) components demonstrates all-weather steam generation, where the CMA can convert sunlight into heat for steam generation and the SC-B can convert sunlight into electricity on sunny days to further power the CMA for electro-thermal steam generation in gloomy weather and dark conditions. This work offers a new co-gelation strategy for the assembly of 2D MXene sheets into highly electrically conductive and highly light-absorbing 3D MXene aerogels and offers new insights to design high-efficiency, all-weather applicable steam generators running in any complex environments for practical applications.

2. Results and discussion

Fig. 1a schematically illustrates the concept of design for all-weather water evaporation. Based on the combined or alternative photo-thermal and electro-thermal conversion process, the steam generation system combined with the solar cells-battery (SC-B) components can achieve all-weather and continuous steam generation. In detail, the CMA converts sunlight into heat for steam generation and solar cells convert sunlight into electricity, respectively, during sunny days, and the electricity stored in the battery further powers the CMA for electro-thermal steam generation under dusky light or dark conditions. In order to meet these criteria, a monolithic porous material with both excellent electrical conductivity and outstanding light absorption performance is necessary. Here, the co-gelation assembly strategy is employed to prepare the crosslinked MXene aerogels, as shown schematically in Fig. 1b. As MXene flakes intrinsically have small size and rigidness, GO sheets with strong gelation capability are utilized as an assistant gelation agent. To avoid the excessive volume shrinkage during assembly, a weak reducing agent EDA is introduced into the MXene/GO colloidal solution to initiate the sheet assembly into a three-dimensional network.[53] Attributed to the ring-opening reaction, hydrogen bonding and electrostatic interactions, EDA can simultaneously crosslink both GO and MXene, resulting in a co-gelation assembly of MXene and GO sheets.

$Ti_3C_2T_x$ MXene sheets were synthesized by selective etching of the Ti_3AlC_2 precursor materials (Fig. S1a, ESI†), followed by sonication and centrifugation *via* a previously reported method.[54] The transmission electron microscopy (TEM) image shows that the delaminated MXene sheets with a lateral size of roughly hundreds of nanometers are ultrathin and transparent, and the selected area electron diffraction (SAED) pattern with a typical hexagonal symmetry reveals the polycrystalline feature of $Ti_3C_2T_x$ MXene sheets (Fig. S1b, ESI†). The AFM image of MXene sheets reveals that the delaminated MXene sheets with a thickness of a few nanometers contain several single layers (Fig. S1c and d, ESI†). The successful synthesis of delaminated MXene sheets was also evidenced by the shift of the (002) lattice X-ray diffraction peak to a smaller angle and the greatly weakened characteristic peaks of Ti_3AlC_2 (Fig. S1e, ESI†).

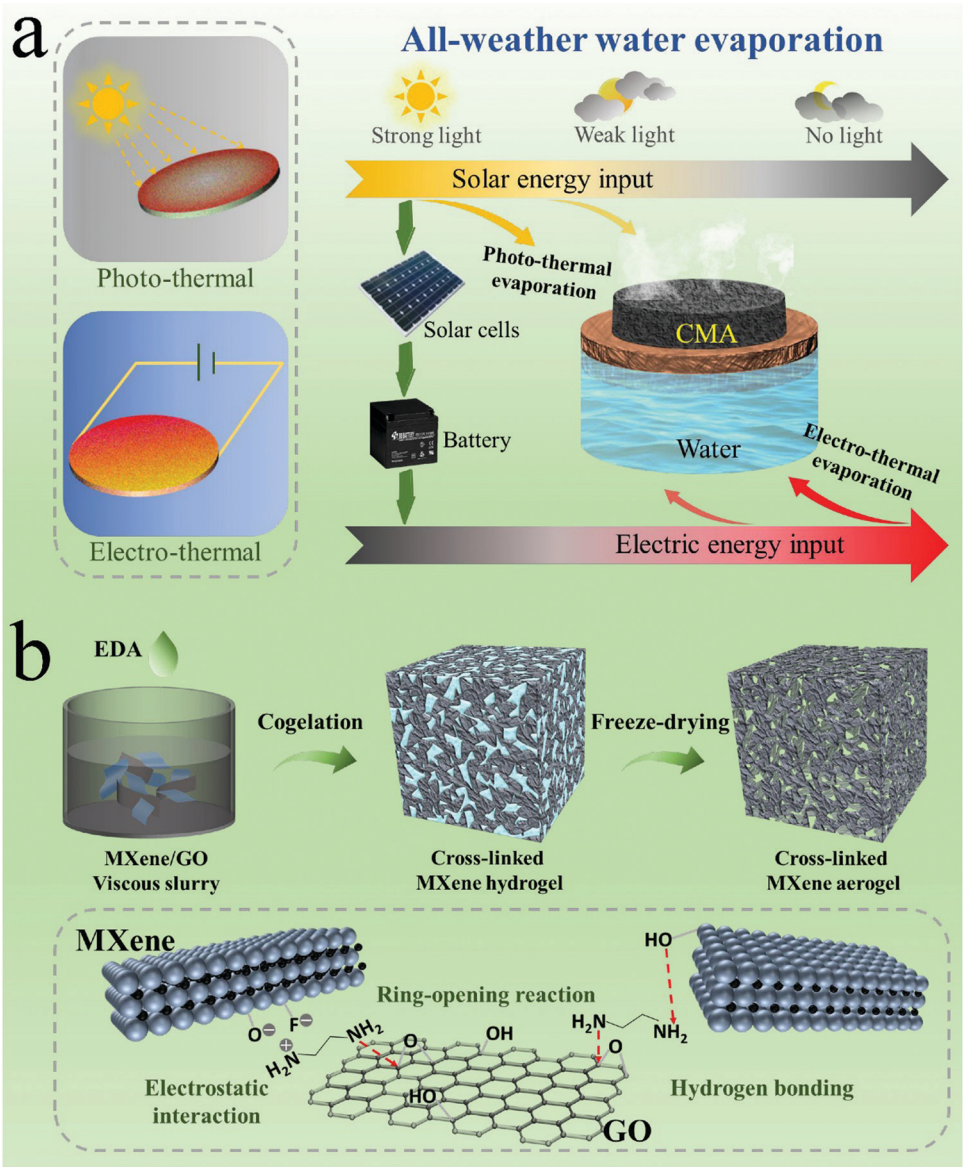

Fig. 1 (a) Conceptual schematic of the all-weather steam generation system based on the synergistic photo-thermal and electro-thermal conversion of CMAs. (b) Schematic illustration for the fabrication process of crosslinked MXene aerogels by GO-assisted co-gelation assembly followed by freeze-drying.

The intrinsic advantages of GO, such as its strong gelation ability, large size and outstanding mechanical flexibility make it particularly suitable for assisting 2D MXene sheets to form 3D MXene architectures.[48] However, using strong reducing agents inevitably causes excessive restacking of the graphene sheets during assembly, manifesting as a macroscopic volume shrinkage[55,56] and resulting in a severely decreased overall efficiency (*e.g.* light absorption, water transportation, *etc.*) of the aerogels. Moreover, the MXene sheets were forcibly wrapped inside the formed reduced graphene oxide (rGO) porous structure during the rapid gelation process, thus the proportion of MXene in the hybrid aerogel could not be improved to a higher level. In order to suppress the restacking of graphene sheets during assembly, a weak reducing agent EDA with crosslinking ability was employed to initiate the assembly process in this work and the CMHs could be easily formed even though the MXene content in the initial MXene/GO suspension was as high as 90%.

As shown in Fig. 2a, a monolithic hydrogel was generated from the MXene/GO–EDA precursor along with certain volume shrinkage due to the effective reduction of GO to rGO by virtue of the reduction ability of MXene.[49] In comparison, no monolithic hydrogel can be formed with either the MXene–EDA or the GO–EDA precursor under the same conditions (the GO–EDA precursor is capable of forming a hydrogel, but its strength is extremely weak), caused by the weak reduction ability of EDA. However, due to the crosslinking capability of EDA with double reaction sites ($-NH_2$), the co-gelation assembly gives rise to a crosslinked hydrogel with superior strength (Fig. 2b). After a subsequent freeze-drying process, the formed high-strength

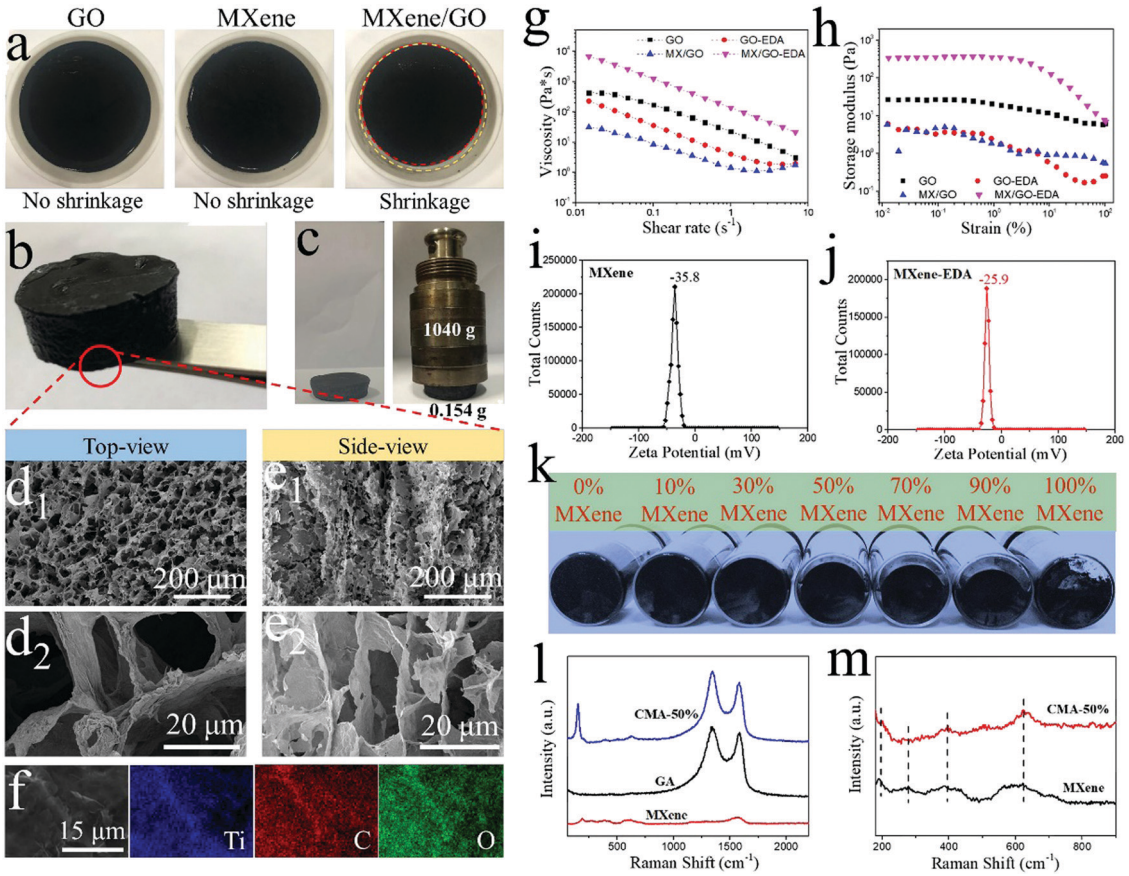

Fig. 2 (a) Optical photographs of GO–EDA, MXene–EDA, and MXene/GO–EDA precursors after hydrothermal assembly under EDA initiation. Optical photographs of (b) a monolithic CMH and (c) CMA (154 mg) supporting a weight of more than 1000 g. (d_1 and d_2) Top-view and (e_1 and e_2) side-view SEM images at different magnifications of CMA. (f) SEM image and corresponding EDS elemental mappings of Ti, C, and O in CMA. Rheological properties of GO, MXene/GO suspensions before and after the addition of EDA with (g) viscosity plotted as a function of shear rate and (h) storage modulus plotted as a function of strain. Zeta potential of the MXene suspension (i) before and (j) after the addition of EDA. (k) Optical photographs of the hydrogels prepared with different contents of MXene. (l) Raman spectra of MXene, GA, and CMA-50%; and (m) high-resolution Raman spectra of MXene and CMA-50%.

skeleton of a CMA with 154 mg can support a load of more than 1 kg without fracture (Fig. 2c). As shown in Fig. 2d and e, an overall aligned cellular structure is obtained when unidirectional freezing and subsequent freeze-drying are used to remove the water from the hydrogel for facilitating the water transport and release of steam during the steam generation process.[57] The elemental mappings in Fig. 2f show uniform distributions of Ti, C, and O elements in the CMA. The retained (002) peak in the XRD patterns of the CMA indicates the well preserved structure of MXene sheets after hydrothermal co-gelation assembly (Fig. S2, ESI†).

To explore the co-gelation mechanisms of MXene sheets and GO sheets, the rheological behaviors of GO and GO/MXene suspensions before and after the addition of EDA were evaluated to determine the viscosity and network variation of the suspensions. All specimens exhibit non-Newtonian characteristics and shear-thinning behavior, and the apparent viscosity (η, Pa s) decreases with shear rate (γ, s^{-1}), as demonstrated in Fig. 2g. The apparent viscosity of the GO/MXene suspension is increased by three orders of magnitude after the addition of EDA, much higher than that of the GO–EDA suspension. This is consistent with the intuitive phenomenon that the GO/MXene suspension becomes more viscous and even loses fluidity after adding EDA, while the individual GO or MXene suspension maintains good fluidity (Fig. S3, ESI†). The storage modulus in these viscoelastic suspensions was plotted as a function of strain, showing much higher storage modulus and longer strain-independent plateau in GO/MXene–EDA (Fig. 2h). Such a rheological behavior in the GO/MXene–EDA suspension indicates that the addition of EDA can cause co-crosslinking of MXene and GO sheets and the formation of the developed crosslinked network structure.

The fact that GO can be crosslinked by EDA through an EDA-mediated nucleophilic ring-opening reaction of epoxy groups on the surface of GO has been evidenced.[53,58] Two aspects, namely, hydrogen bonding and electrostatic interaction, may contribute to the crosslinking of MXene by EDA. On the one hand, the typical –OH peak of MXene at 546 cm^{-1} shifts to a lower wavenumber, indicating the formation of hydrogen bonds between –OH of MXene and $-NH_2$ of EDA (Fig. S4, ESI†). On the other hand, the $Ti_3C_2T_x$ MXene is negatively charged owing to the presence of the surface functional groups (–OH, –F, and –O),

while $-NH_2$ is positively charged. After the addition of EDA, the zeta potential of the MXene suspension increased from −35.8 mV to −25.9 mV (Fig. 2i and j). As seen in Fig. S5 (ESI†), after being subjected to a reaction at 80 °C for 2 hours, the mixed MXene–EDA suspension became extremely viscous due to the mild reaction between MXene and EDA.

GO is crucial for assembling MXene sheets into crosslinked aerogels. A series of MXene/GO precursors with different MXene contents have been assembled into crosslinked MXene hydrogels (CMH-*x*, where *x* represents the proportion of MXene in the hybrid suspensions) with differential volume shrinkage even with MXene content up to 90%, as demonstrated in Fig. 2k. The reduction ability of MXene plays a key role in the partial reduction of GO and thus leads to volume shrinkage. High-resolution X-ray photoelectron spectroscopy (XPS) patterns of Ti 2p show that the intensity of the peak assigned to TiO_2 is significantly increased, which indicates the oxidation of $Ti_3C_2T_x$ MXene during the assembly process (Fig. S6, ESI†). The appearance of the characteristic peak of TiO_2 in the Raman spectrum further confirms the oxidation of MXene (Fig. 2l). Despite this, the peaks assigned to MXene are still preserved in the Raman spectrum (Fig. 2m). With increasing content of MXene, a more contracted hydrogel is obtained because of a higher degree reduction of GO. However, MXene hydrogels cannot be obtained without the assistance of GO owing to the weak gelation capability of MXene. Interestingly, no monolithic hydrogel is formed without EDA because a large amount of MXene cannot be wrapped inside the skeleton during the rapid reduction process of GO, when the MXene content reaches 70% (Fig. S7, ESI†). This indicates that EDA is critical for the fabrication of crosslinked MXene hydrogels.

The metal-like characteristic of MXene endows it with excellent electrical conductivity, which leads to efficient electro-thermal conversion. The co-gelation assembly is significantly beneficial to the electrical conductivity of CMAs, harnessing the intrinsically high conductivity of MXene. As seen in Fig. 3a, with the content of MXene increasing, the electrical conductivity of the CMAs increases in orders of magnitude, reaching a value as high as 140 S m^{-1} for the CMA with an MXene content of 90%. Furthermore, CMA-90% demonstrates higher electrical conductivity upon further increasing the density of aerogels, such as 200, 307, and 430 S m^{-1} for CMA-90% with densities of 21, 26, and 32 mg cm^{-3}, respectively (Fig. 3b). These outstanding conductivities are significantly higher than those of reported porous carbon materials, such as 87 S m^{-1} for a graphene aerogel (10 mg cm^{-3}),[59] and 20 S m^{-1} for a carbon nanotube foam (60 mg cm^{-3}).[60] The electro-thermal properties of CMAs with different contents of MXene were investigated. Fig. S8 (ESI†) shows the various infrared (IR) thermal images for different CMAs with different contents of MXene under an applied voltage of 5 V, wherein the heating temperatures are recorded by an IR camera. It can be found that only CMA-90% can be easily driven to a higher temperature, indicating the importance of increasing the content of MXene in the hybrid aerogels. Fig. 3c shows the generated temperature profiles of CMA-90% with variations of the applied voltage. Specially, for the CMA-90 sample with a low resistance of ∼6 Ω, a small voltage supply of 3 V can cause a high temperature of nearly 110 °C due to the extremely high electrical conductivity of the crosslinked MXene aerogel. Fig. 3d shows the IR thermal images of two different CMA-90% samples with different resistances due to their different densities when an identical voltage of 3 V was applied for different times. The lower resistance sample (∼6 Ω) can attain a higher temperature more easily than that with a higher resistance (∼28 Ω) (Fig. 3d_1 and d_2), indicating high electrical conductivity is crucial for the electro-thermal performance.

In addition to the electro-thermal conversion, photo-thermal conversion performance is equally important to develop all-weather steam generators. The photo-thermal conversion of MXene is based on the localized surface plasmon resonance (LSPR) effect of Ti_3C_2 nanosheets,[61] which is similar to the metal nanoparticles such as Au, Ag, *etc.* Aerogel surface temperature under simulated light illumination was recorded by an IR camera for the evaluation of photo-thermal conversion performance, as schematically illustrated in Fig. 3e. The light absorption spectra in Fig. 3f show that the CMA sample exhibits higher light absorption efficiency (∼99%) compared with the GA sample due to the better light absorption capability of MXene sheets. This can also be evidenced by the optical photographs in the inset of Fig. 3f, where the CMA sample looks apparently darker than the GA sample. Increasing the power density of solar illumination from 1 to 5 kW m^{-2}, the surface temperature change (ΔT) of the CMA increases from 80 to 235 °C (Fig. 3g). Under the same solar illumination, the CMA always has a surface temperature higher than that of the GA, further indicating the superior photo-thermal conversion of the CMA.

Given that the sun position always changes in practice, less dependence on the light incident direction is also a fundamental requirement for solar energy utilization. The surface temperatures of different samples under 1 kW m^{-2} solar illumination with varied incident angles were measured (Fig. 3h). The GA and CMA samples maintain good photo-thermal conversion stability with a slight decrease in temperature as the incident angle increases from 0° to 70° as shown in Fig. 3i. In comparison, the surface temperature of the M/G aerogel free of EDA decreases sharply when the incident angle increases to 70° (Fig. S9a, ESI†). This is because the interconnected network forms based on the crosslinking of MXene and GO sheets induced by EDA. The porous structure enhances the light absorption by elongating the optical path for multiple reflections (Fig. 3j). However, the denser structure and flatter surface formed due to the reduction of GO to rGO and severe π–π stacking in the absence of EDA (Fig. S9b, ESI†) result in the restriction of light-shielding effect and insufficient utilization of incident light.[62] These results demonstrate the advantages of CMAs for the maximization of solar utilization.

Besides, hydrophilic wettability and water supply capacity play important roles in rapid water transportation for highly efficient solar-steam conversion.[63–66] Unlike other 2D materials, the delaminated MXene sheets with the termination T_x (*e.g.* –OH, –F, and –O)

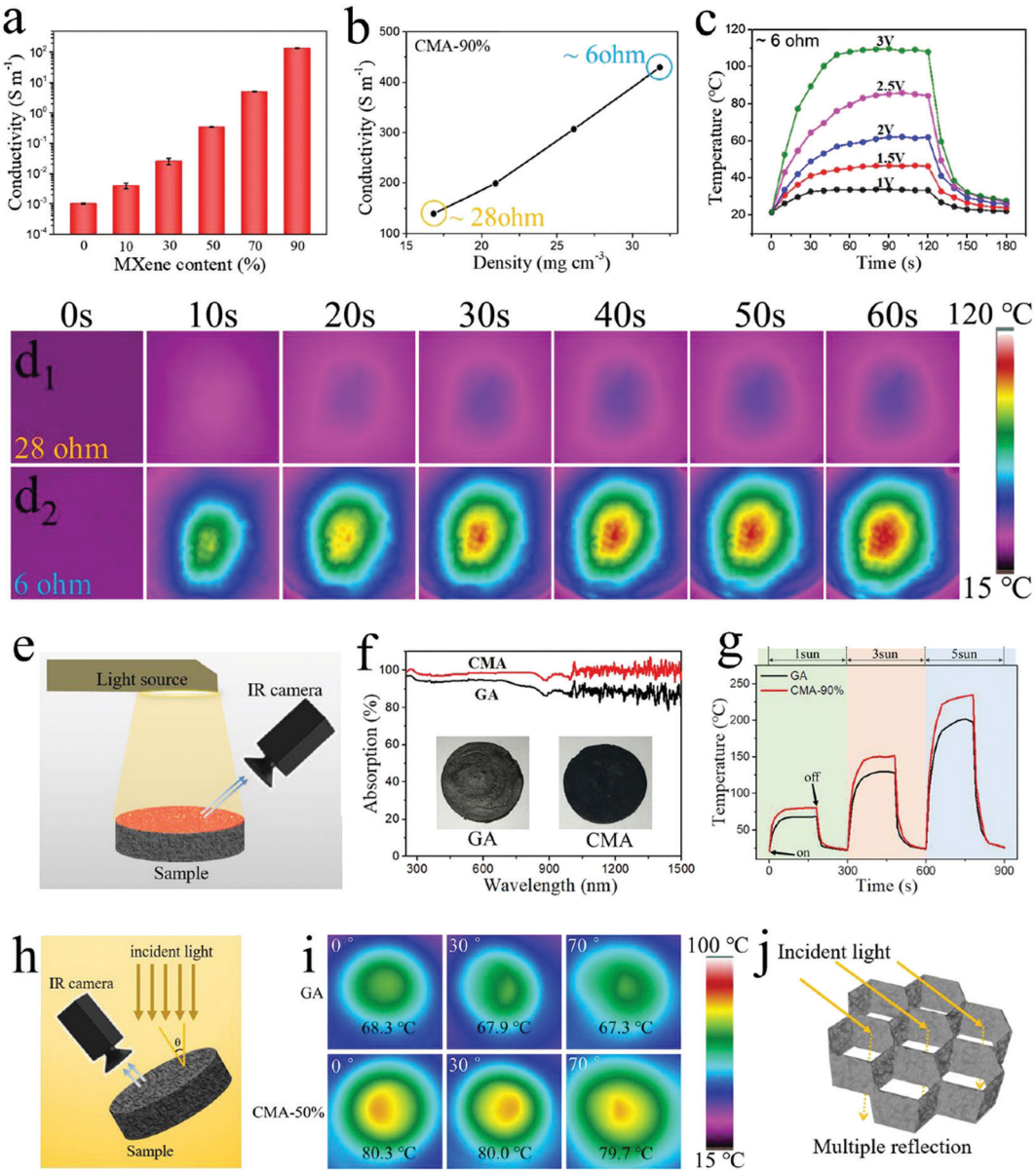

Fig. 3 Electrical conductivities of (a) CMA with different contents of MXene, and (b) CMA-90% with different densities. (c) Temperature evolution of the CMA-90% (32 mg cm^{-3}) sample with a resistance of ~6 Ω under different voltages. (d) IR thermal images of two different CMA-90% samples with different resistances when an identical voltage of 3 V was applied for different time periods. (e) Schematic illustration for photo-thermal conversion measurement. (f) The light absorption spectra for the GA and CMA samples. The inset in (f) shows the optical photographs of the GA and CMA samples. (g) The temperature changing course of the GA and CMA samples under solar illumination of 1, 3, and 5 kW m^{-2}, turned on and off. (h) Schematic illustration for photo-thermal conversion measurements at different incident angles. (i) IR thermal images of GA and CMA at varied incident angles (0°, 30°, and 70°) after reaching a stable temperature state under solar illumination of 1 kW m^{-2}. (j) Schematic illustration for multiple reflection of incident light in the porous structure.

have unique hydrophilicity, endowing the as-prepared composite aerogels with hydrophilic surfaces and facile water wettability, thus facilitating water transportation. From this point of view, the termination T_x can affect the water transportation and thus ensure the water evaporation performance. To further confirm the wettability of the as-prepared CMA, a high-speed video camera was used to record the impregnation process. As shown in Fig. S10a (ESI†), the CMA shows super hydrophilic properties and the droplet can be fully impregnated within 5 s, indicating its excellent water transportation properties. In contrast, the impregnation process of the M/G aerogel free of EDA is very slow and the droplet cannot be fully impregnated due to the dense surface caused by the excessive stacking between sheets (Fig. S10b, ESI†). As the as-prepared CMA with excellent hydrophilic properties is unable to float at the water–air interface spontaneously, a piece of wood is used to support it for floating. Additionally, to reduce the heat loss to the underlying water during the solar-driven steam generation,

it is essential to make sure that photothermal materials have low thermal conductivity for effective heat localization. Herein, we visually compared the thermal insulation properties of the as-prepared CMA with several commercial thermal insulation materials including polyvinyl alcohol (PVA) foam, polyurethane (PU) foam, and melamine foam (MF). To avoid the effect of inhomogeneous temperature on the heating platform surface, a nitrile butadiene rubber (NBR) board was placed on the heating platform, and the samples were placed on the NBR board (Fig. S11a, ESI†). The temperature of the heating platform was set to be 50, 100 and 140 °C, and IR thermal images of the samples captured at 5 min are presented in Fig. S11b–d (ESI†). When the actual temperature of the heating platform reaches high temperatures, *i.e.*, 50, 100, and 140 °C, the detected temperatures on the CMA is just ~30.2, ~38.4 and ~50.2 °C correspondingly, indicating its good thermal insulation properties. Apparently, the CMA has comparable thermal insulation properties with those of commercial thermal insulation materials.

Despite the remarkable advancements of solar-driven steam generation achieved under strong solar illumination (≥1 sun) in recent years, in fact, it is still challenging to achieve great energy conversion efficiency under weak solar illumination (<1 sun) due to the low surface temperature. Given that 80% of the time in one day is filled with low light or darkness, it is necessary to improve the energy efficiency under these conditions. So, electro-thermal conversion can be introduced to increase the CMA surface temperature on the basis of photothermal conversion. A combination of different voltages (*i.e.*, 1, 1.5, 2, and 2.5 V) and different light energies (*i.e.*, 0.5, 0.7, and 1 sun) was input to CMA-90%, and the IR thermal images of the sample captured at steady states are presented in Fig. 4a. Benefiting from the high electrical conductivity of CMA-90%, the low voltage supply of 2.5 V in conjunction with the low solar illumination of 0.5 sun can significantly generate a higher surface temperature compared to the only 1 sun solar illumination case without the voltage supply. These results indicate that coupling photo-thermal and electro-thermal conversion is a promising strategy to elevate the sample surface temperature for facilitating steam generation.

In a typical all-weather prototype, only solar energy is utilized to drive steam generation on sunny days (strong light), combined solar energy and electrical energy can be utilized to drive steam generation on cloudy days (weak light), and only electrical energy can be utilized to drive steam generation at nights (dark), as schematically demonstrated in Fig. 4b–d. The evaporation rate and energy conversion efficiency of CMA-90% was measured under only solar illumination of different intensities, combining solar energy and electrical energy with different voltages, and only electrical energy input with different voltages.

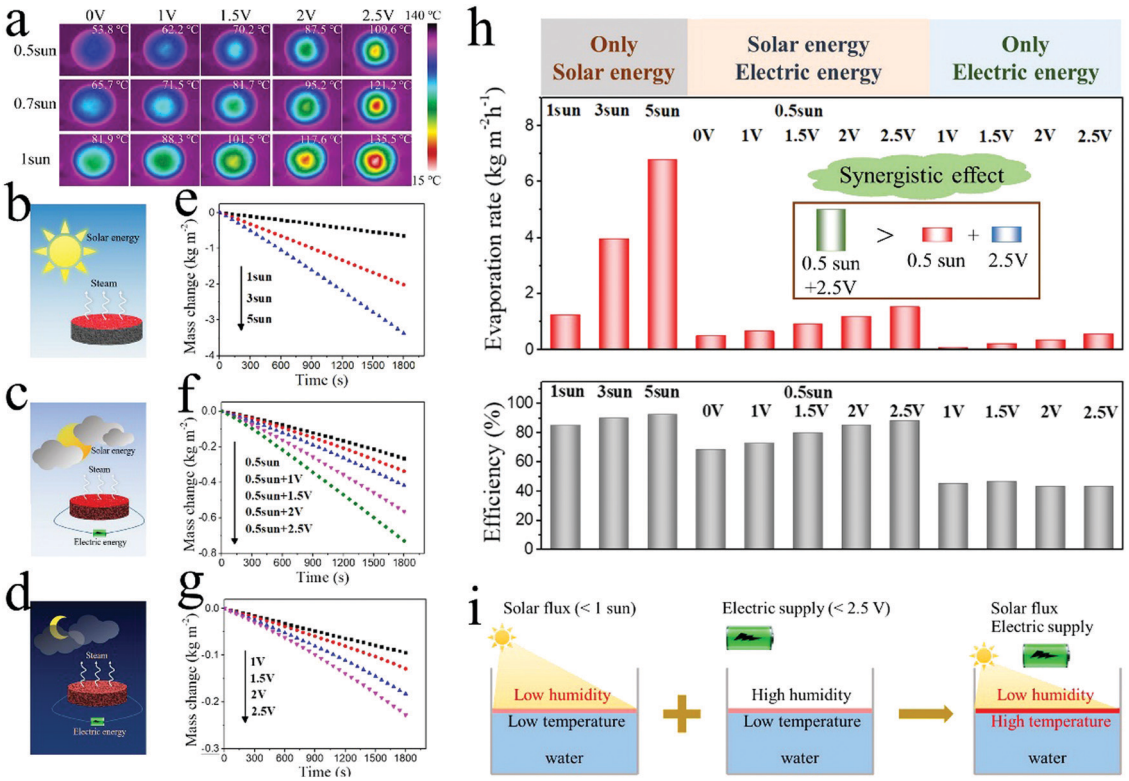

Fig. 4 (a) IR thermal images of CMAs under different total energy inputs combining different electrical energies (*i.e.*, 1, 1.5, 2, and 2.5 V) and different light energies (*i.e.*, 0.5, 0.7, and 1 sun). Schematic illustration of steam generation under different environments from (b) sunny days (strong-light condition), (c) cloudy days (low-light condition), (d) and nighttime (dark condition). The mass change of water under different energy inputs of (e) only solar illumination, (f) combined solar and electricity, and (g) only voltage supply. (h) The water evaporation rate and efficiency under all conditions. (i) Schematic illustrations showing the synergistic effect between solar flux and electric supply.

As shown in Fig. 4e, the water evaporation rate gradually increases with increasing solar illumination intensity from 1 sun to 5 sun. When the intensity of solar illumination is set as 0.5 sun, the water evaporation rate gradually increases with increasing voltage supply (Fig. 4f). Remarkably, the water evaporation rate under the low solar energy (0.5 sun) coupled with some electrical energy (2.5 V voltage supply) input is higher than that under only solar illumination of 1 sun. Furthermore, without solar illumination, the water evaporation rate gradually increases as the voltage supply increases from 1 V to 2.5 V (Fig. 4g). It is worth noting that the resistance of CMAs slightly increases during the water evaporation process due to the impact of water on the porous structure, as shown in Fig. S12 (ESI†), while it is negligible for electro-thermal conversion.

The energy conversion (from solar energy and electrical energy to steam enthalpy) efficiency is defined as $\eta = \nu h_{LV}/Q_{in}$, where η is the energy conversion efficiency, ν is the water evaporation rate, h_{LV} is the total enthalpy of sensible heat (Q_S, J g^{-1}) and the phase transition of liquid–vapor (L_V, J g^{-1}), and Q_{in} is the total energy input including solar energy and electrical energy. The calculated water evaporation rates and energy conversion efficiencies for all conditions including only solar energy input, combined solar and electrical energy input, and sole electrical energy input, are presented in Fig. 4h. Although relatively high evaporation rates can be obtained under strong solar illumination of 3 sun or 5 sun, it is more meaningful to focus on the evaporation rate under weak solar illumination with low intensity (such as 0.5 sun) considering the low light illumination conditions in practice, *e.g.* cloudy days or darkness. Under solar illumination of 0.5 sun, the evaporation rate is significantly increased with a low voltage supply, and even higher than that under 1 sun solar illumination. Interestingly, a synergistic effect of solar and electrical energy driven steam generation can be found, as shown by the inset of Fig. 4h, where the evaporation rate under the combined solar energy of 0.5 sun and electrical energy of 2.5 V is higher than the sum of the evaporation rates under only solar illumination of 0.5 sun and only 2.5 V voltage supply. Therefore, the

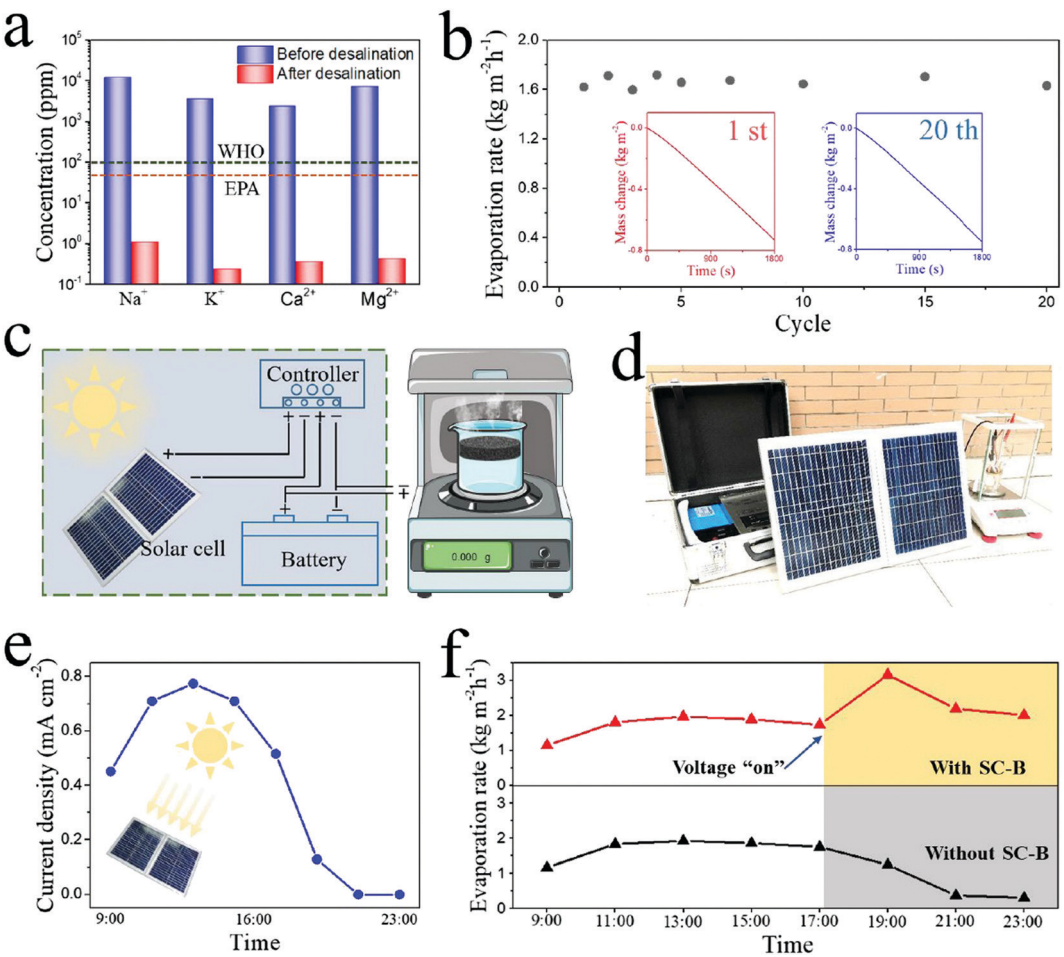

Fig. 5 (a) The measured concentrations of four primary ions in a standard seawater sample before (original) and after evaporation desalination. (b) The water evaporation durability performance of CMA under the combined solar illumination of 0.5 sun and voltage supply of 5 V over 20 cycles. Insets: The mass change of water with the CMA in the 1st cycle and 20th cycle. (c) Schematic illustration showing that the solar cells convert sunlight into electricity and store it into battery for further powering the steam generator. (d) Optical photographs of a set of large-scale steam generation system. (e) The charging current density of SC-B components at different times from 9:00 am to 23:00 pm. (f) The water evaporation rates at different times in two situations, that is with SC-B or without SC-B.

great energy conversion efficiency of 88.4% can be obtained for the system with combined solar and electrical energy input, much higher than that with only solar illumination of 0.5 sun (68.6%) and that with sole 2.5 V voltage supply (43.4%). This synergistic effect can be explained as follows: (1) the electrical energy input can increase the surface temperature of samples; (2) solar illumination reduces the humidity of the system above the sample, as schematically shown in Fig. 4i. These two factors promote the liquid water–steam conversion and the escape of steam.

A standard seawater sample was used to evaluate the desalination performance of the CMAs. The results in Fig. 5a show that the concentrations of the four primary ions of Na^+, K^+, Ca^{2+} and Mg^{2+} determined using inductively coupled plasma optical emission spectroscopy (ICP-OES) significantly decrease with an ion rejection beyond 99% after desalination with CMA-90%. Meanwhile, the Na^+ ion concentration is below the salinity levels defined by the World Health Organization (WHO) and the standards of the US Environmental Protection Agency (EPA). The photo-corrosion of semiconductors is a critical issue under the practical condition with oxygen and water. Fortunately, the TiO_2 produced by partial oxidation of MXene has excellent stability, because the titanium ions have poor activity and are difficult to react with photogenerated electron–hole pairs. In addition, the prepared MXene-based aerogels with partial oxidation exhibit excellent light absorption efficiency of up to 99%, indicating that the formed TiO_2 did not affect the original photothermal conversion performance of MXene. To prove the durability of the CMA as a steam generator, we tested the steady evaporation rate under the combined solar illumination of 0.5 sun and voltage supply of 5 V over 20 cycles (Fig. 5b). The high-resolution Raman spectra of CMAs before and after evaporation in Fig. S13 (ESI†) indicated that the degree of further oxidation of MXene is low during water evaporation. The stable evaporation rate shows that the CMA presents a promising performance for practical long-term desalination.

In order to make full use of solar energy without using additional electrical energy supply devices in all-weather and continuous steam generation processes, SC-B components were introduced to convert sunlight into electricity on sunny days and to store it in the battery for further powering the CMA to continuously generate steam, as schematically shown in Fig. 5c. To examine the practical performance of the CMA, a large-scale system was designed and fabricated (Fig. 5d). The system was placed in the outdoor environment and the recorded charging current density of SC-B components during 14 hours of one day from 9:00 am to 23:00 pm is presented in Fig. 5e, indicating the varying sunlight illumination in one day. The output voltage of the battery is set to 12 V. The CMA under natural sunlight illumination continuously generates steam, and the solar cells convert sunlight into electricity and store it into the battery from 9:00 am to 18:00 pm. When the light intensity became weak at 18:00 pm, insufficient to effectively generate current, the voltage output switch was turned on and the SC-B components began to power the CMA for continuously generating steam from 18:00 to 23:00 pm. Fig. 5f shows that the evaporation rate can reach more than 3 kg m^{-2} h^{-1} after turning on the voltage output switch, and a much higher total evaporation rate of 29.4 kg m^{-2} can be achieved after 14 h compared to that (19.2 kg m^{-2}) without the SC-B components. Based on the above results, it is reasonable to conclude that the steam generation system consisting of CMA and SC-B can promote the development of all-weather and continuous steam generation devices running in any complex environments for practical applications.

3. Conclusion

We have demonstrated an all-weather-available and continuous steam generation system based on macroscopic MXene architectures. The as-prepared crosslinked MXene aerogels on the basis of the novel co-gelation assembly strategy can work well for photo-thermal and electro-thermal conversion, while having excellent hydrophilic properties and thermal insulation performance. In virtue of the synergistic coupling of photo-thermal and electro-thermal processes, a high evaporation rate (1.624 kg m^{-2} h^{-1}) can be achieved under the combined energy input of 0.5 kW m^{-2} light energy and 2.5 V voltage supply, much higher than that (1.337 kg m^{-2} h^{-1}) under 1 kW m^{-2} light energy input. Combined with SC-B components, the steam generation system can harvest solar energy to continuously generate steam based on the alternating photo-thermal and electro-thermal conversion of CMAs at all hours of day and night, and can deliver a high evaporation rate of 29.4 kg m^{-2} in 14 hours of a day. This work not only offers a new co-gelation strategy for the assembly of 2D MXene sheets into highly electrically conductive and highly light-absorbing 3D MXene aerogels, but also proposes new insights toward designing high-efficiency, all-weather-applicable steam generators running in any complex environments for practical applications.

Conflicts of interest

There are no conflicts to declare.

Acknowledgements

The authors gratefully acknowledge the financial support from the National Natural Science Foundation of China (NNSFC grants 51873126, 51422305 and 51721091).

References

1 A. E. Kabeel and S. A. El-Agouz, *Desalination*, 2011, **276**, 1–12.
2 P. Tao, G. Ni, C. Y. Song, W. Shang, J. B. Wu, J. Zhu, G. Chen and T. Deng, *Nat. Energy*, 2018, **3**, 1031–1041.
3 Z. T. Li, C. B. Wang, J. B. Su, S. Ling, W. Wang and M. An, *Sol. RRL*, 2019, **3**, 1800206.
4 H. Ghasemi, G. Ni, A. M. Marconnet, J. Loomis, S. Yerci, N. Miljkovic and G. Chen, *Nat. Commun.*, 2014, **5**, 4449.

5 Y. Ito, Y. Tanabe, J. Han, T. Fujita, K. Tanigaki and M. Chen, *Adv. Mater.*, 2015, **27**, 4302–4307.
6 Z. C. Xiong, Y. J. Zhu, D. D. Qin, F. F. Chen and R. L. Yang, *Small*, 2018, **14**, e1803387.
7 F. Gong, H. Li, W. Wang, J. Huang, D. Xia, J. Liao, M. Wu and D. V. Papavassiliou, *Nano Energy*, 2019, **58**, 322–330.
8 L. Zhu, T. Ding, M. Gao, C. K. N. Peh and G. W. Ho, *Adv. Energy Mater.*, 2019, **9**, 1900250.
9 X. Y. Zhou, F. Zhao, Y. H. Guo, Y. Zhang and G. H. Yu, *Energy Environ. Sci.*, 2018, **11**, 1985–1992.
10 Z. Liu, B. Wu, B. Zhu, Z. Chen, M. Zhu and X. Liu, *Adv. Funct. Mater.*, 2019, **29**, 1905485.
11 T. T. Li, Q. L. Fang, X. F. Xi, Y. S. Chen and F. Liu, *J. Mater. Chem. A*, 2019, **7**, 586–593.
12 X. Yang, Y. Yang, L. Fu, M. Zou, Z. Li, A. Cao and Q. Yuan, *Adv. Funct. Mater.*, 2018, **28**, 1704505.
13 X. Hu, W. Xu, L. Zhou, Y. Tan, Y. Wang, S. Zhu and J. Zhu, *Adv. Mater.*, 2017, **29**, 1604031.
14 Y. Yang, R. Zhao, T. Zhang, K. Zhao, P. Xiao, Y. Ma, P. M. Ajayan, G. Shi and Y. Chen, *ACS Nano*, 2018, **12**, 829–835.
15 M. W. Zhu, Y. J. Li, F. J. Chen, X. Y. Zhu, J. Q. Dai, Y. F. Li, Z. Yang, X. J. Yan, J. W. Song, Y. B. Wang, E. Hitz, W. Luo, M. H. Lu, B. Yang and L. B. Hu, *Adv. Energy Mater.*, 2018, **8**, 1701028.
16 Z. Sun, J. Wang, Q. Wu, Z. Wang, Z. Wang, J. Sun and C.-J. Liu, *Adv. Funct. Mater.*, 2019, **29**, 1901312.
17 L. Cui, P. Zhang, Y. Xiao, Y. Liang, H. Liang, Z. Cheng and L. Qu, *Adv. Mater.*, 2018, **30**, e1706805.
18 X. Ma, W. Fang, Y. Guo, Z. Li, D. Chen, W. Ying, Z. Xu, C. Gao and X. Peng, *Small*, 2019, **15**, e1900354.
19 Z. Z. Wang, Q. X. Ye, X. B. Liang, J. L. Xu, C. Chang, C. Y. Song, W. Shang, J. B. Wu, P. Tao and T. Deng, *J. Mater. Chem. A*, 2017, **5**, 16359–16368.
20 A. Guo, X. Ming, Y. Fu, G. Wang and X. Wang, *ACS Appl. Mater. Interfaces*, 2017, **9**, 29958–29964.
21 D. Ghim, Q. S. Jiang, S. S. Cao, S. Singamaneni and Y. S. Jun, *Nano Energy*, 2018, **53**, 949–957.
22 Y. W. Yang, H. Y. Zhao, Z. Y. Yin, J. Q. Zhao, X. T. Yin, N. Li, D. D. Yin, Y. N. Li, B. Lei, Y. P. Du and W. X. Que, *Mater. Horiz.*, 2018, **5**, 1143–1150.
23 Z. Zhang, P. Mu, J. Han, J. He, Z. Zhu, H. Sun, W. Liang and A. Li, *J. Mater. Chem. A*, 2019, **7**, 18092–18099.
24 H. W. Liu, C. J. Chen, H. Wen, R. X. Guo, N. A. Williams, B. D. Wang, F. J. Chen and L. B. Hu, *J. Mater. Chem. A*, 2018, **6**, 18839–18846.
25 X. Zhou, F. Zhao, Y. Guo, B. Rosenberger and G. Yu, *Sci. Adv.*, 2019, **5**, eaaw5484.
26 C. Tu, W. Cai, X. Chen, X. Ouyang, H. Zhang and Z. Zhang, *Small*, 2019, **15**, 1902070.
27 C. Li, D. Jiang, B. Huo, M. Ding, C. Huang, D. Jia, H. Li, C. Liu and J. Liu, *Nano Energy*, 2019, **60**, 841–849.
28 M. Tan, J. Wang, W. Song, J. Fang and X. Zhang, *J. Mater. Chem. A*, 2019, **7**, 1244–1251.
29 L. Zhu, L. Sun, H. Zhang, D. Yu, H. Aslan, J. Zhao, Z. Li, M. Yu, F. Besenbacher and Y. Sun, *Nano Energy*, 2019, **57**, 842–850.
30 X. Wu, M. E. Robson, J. L. Phelps, J. S. Tan, B. Shao, G. Owens and H. L. Xu, *Nano Energy*, 2019, **56**, 708–715.
31 F. Liu, B. Zhao, W. Wu, H. Yang, Y. Ning, Y. Lai and R. Bradley, *Adv. Funct. Mater.*, 2018, **28**, 1803266.
32 S. Choi, J. Park, W. Hyun, J. Kim, J. Kim, Y. B. Lee, C. Song, H. J. Hwang, J. H. Kim, T. Hyeon and D.-H. Kim, *ACS Nano*, 2015, **9**, 6626–6633.
33 P. Zhang, J. Li, L. Lv, Y. Zhao and L. Qu, *ACS Nano*, 2017, **11**, 5087–5093.
34 X. Xie, M.-Q. Zhao, B. Anasori, K. Maleski, C. E. Ren, J. Li, B. W. Byles, E. Pomerantseva, G. Wang and Y. Gogotsi, *Nano Energy*, 2016, **26**, 513–523.
35 M. Naguib, M. Kurtoglu, V. Presser, J. Lu, J. Niu, M. Heon, L. Hultman, Y. Gogotsi and M. W. Barsoum, *Adv. Mater.*, 2011, **23**, 4248–4253.
36 M. Naguib, V. N. Mochalin, M. W. Barsoum and Y. Gogotsi, *Adv. Mater.*, 2014, **26**, 992–1005.
37 J. Zhao, Y. Yang, C. Yang, Y. Tian, Y. Han, J. Liu, X. Yin and W. Que, *J. Mater. Chem. A*, 2018, **6**, 16196–16204.
38 X. Xie, K. Kretschmer, B. Anasori, B. Sun, G. Wang and Y. Gogotsi, *ACS Appl. Nano Mater.*, 2018, **1**, 505–511.
39 X. Xie, C. Chen, N. Zhang, Z.-R. Tang, J. Jiang and Y.-J. Xu, *Nat. Sustain.*, 2019, **2**, 856–862.
40 X. Zhao, X.-J. Zha, J.-H. Pu, L. Bai, R.-Y. Bao, Z.-Y. Liu, M.-B. Yang and W. Yang, *J. Mater. Chem. A*, 2019, **7**, 10446–10455.
41 L. An, P. Mu, W. Bai, Y. Fan, Z. Zhang, H.-X. Sun, Z.-Q. Zhu and W.-D. Liang, *J. Mater. Chem. A*, 2019, **7**, 9673–9679.
42 B. B. Huo, D. G. Jiang, X. Y. Cao, H. Liang, Z. Liu, C. W. Li and J. Q. Liu, *Carbon*, 2019, **142**, 13–19.
43 R. Li, L. Zhang, L. Shi and P. Wang, *ACS Nano*, 2017, **11**, 3752–3759.
44 M. Q. Zhao, X. Xie, C. E. Ren, T. Makaryan, B. Anasori, G. Wang and Y. Gogotsi, *Adv. Mater.*, 2017, **29**, 1702410.
45 M. R. Lukatskaya, O. Mashtalir, C. E. Ren, Y. Dall'Agnese, P. Rozier, P. L. Taberna, M. Naguib, P. Simon, M. W. Barsoum and Y. Gogotsi, *Science*, 2013, **341**, 1502–1505.
46 M. Boota, B. Anasori, C. Voigt, M.-Q. Zhao, M. W. Barsoum and Y. Gogotsi, *Adv. Mater.*, 2016, **28**, 1517–1522.
47 J. Liu, H. B. Zhang, R. Sun, Y. Liu, Z. Liu, A. Zhou and Z. Z. Yu, *Adv. Mater.*, 2017, **29**, 1702367.
48 S. Zhao, H.-B. Zhang, J.-Q. Luo, Q.-W. Wang, B. Xu, S. Hong and Z.-Z. Yu, *ACS Nano*, 2018, **12**, 11193–11202.
49 Y. Chen, X. Xie, X. Xin, Z.-R. Tang and Y.-J. Xu, *ACS Nano*, 2018, **13**, 295–304.
50 Y. Ma, Y. Yue, H. Zhang, F. Cheng, W. Zhao, J. Rao, S. Luo, J. Wang, X. Jiang, Z. Liu, N. Liu and Y. Gao, *ACS Nano*, 2018, **12**, 3209–3216.
51 T. Shang, Z. Lin, C. Qi, X. Liu, P. Li, Y. Tao, Z. Wu, D. Li, P. Simon and Q.-H. Yang, *Adv. Funct. Mater.*, 2019, **29**, 1903960.
52 X. Zhang, R. Lv, A. Wang, W. Guo, X. Liu and J. Luo, *Angew. Chem., Int. Ed.*, 2018, **57**, 15028–15033.
53 H. Hu, Z. Zhao, W. Wan, Y. Gogotsi and J. Qiu, *Adv. Mater.*, 2013, **25**, 2219–2223.
54 M. Alhabeb, K. Maleski, B. Anasori, P. Lelyukh, L. Clark, S. Sin and Y. Gogotsi, *Chem. Mater.*, 2017, **29**, 7633–7644.

55 H. Wang, X. Mi, Y. Li and S. Zhan, *Adv. Mater.*, 2019, 1806843, DOI: 10.1002/adma.201806843.
56 J. Wu, Q. e. Zhang, J. Wang, X. Huang and H. Bai, *Energy Environ. Sci.*, 2018, **11**, 1280–1286.
57 Q. Zhang, H. Yang, X. Xiao, H. Wang, L. Yan, Z. Shi, Y. Chen, W. Xu and X. Wang, *J. Mater. Chem. A*, 2019, **7**, 14620–14628.
58 T. Kuila, S. Bose, A. K. Mishra, P. Khanra, N. H. Kim and J. H. Lee, *Prog. Mater. Sci.*, 2012, **57**, 1061–1105.
59 M. A. Worsley, P. J. Pauzauskie, T. Y. Olson, J. Biener, J. H. Satcher and T. F. Baumann, *J. Am. Chem. Soc.*, 2010, **132**, 14067–14069.
60 M. A. Worsley, S. O. Kucheyev, J. H. S. Jr., A. V. Hamza and T. F. Baumann, *Appl. Phys. Lett.*, 2009, **94**, 073115.
61 H. Lin, X. Wang, L. Yu, Y. Chen and J. Shi, *Nano Lett.*, 2017, **17**, 384–391.
62 X. Xie, N. Zhang, Z.-R. Tang and Y.-J. Xu, *Chem. Sci.*, 2018, **9**, 8876–8882.
63 Y. Jin, J. Chang, Y. Shi, L. Shi, S. Hong and P. Wang, *J. Mater. Chem. A*, 2018, **6**, 7942–7949.
64 P. Zhang, F. Liu, Q. Liao, H. Yao, H. Geng, H. Cheng, C. Li and L. Qu, *Angew. Chem., Int. Ed.*, 2018, **57**, 16343–16347.
65 W. C. Xu, X. Z. Hu, S. D. Zhuang, Y. X. Wang, X. Q. Li, L. Zhou, S. N. Zhu and J. Zhu, *Adv. Energy Mater.*, 2018, **8**, 1702884.
66 P. Mu, Z. Zhang, W. Bai, J. X. He, H. X. Sun, Z. Q. Zhu, W. D. Liang and A. Li, *Adv. Energy Mater.*, 2019, **9**, 1802158.